Evidence of a collision between the Yucatán Block and Mexico in the Miocene

YoungHee Kim,[1]* Robert W. Clayton[1] and Fraser Keppie[2]

[1]*Seismological Laboratory, Division of Geological and Planetary Science, California Institute of Technology, Pasadena, CA 91125, USA.*
E-mail: ykim@caltech.edu
[2]*Department of Natural Resources,* 1701 *Hollis Street, Halifax, Nova Scotia,* B3J2T9, *Canada*

SUMMARY

We present the evidence for an anomalous southwest-dipping slab in southern Mexico. The main evidence comes from a clear receiver function image along a seismic line across the Isthmus of Tehuantepec and is also supported by a previous global tomographic model. The slab dips at 35°, is approximately 250 km in length and appears to truncate the Cocos slab at about 120 km depth. We hypothesize that the slab was created by subduction of oceanic lithosphere prior to the collision of the Yucatán Block with Mexico at approximately 12 Ma. This scenario would explain the Chiapas Fold and Thrust Belt as the product of this collision, and its age constrains the date of the event to be in the Miocene.

Key words: Seismicity and tectonics; Body waves; Seismic tomography; Subduction zone processes; Dynamics of lithosphere and mantle; Dynamics: seismotectonics.

1 INTRODUCTION

Southern Mexico is a transition zone between the flat slab subduction of central Mexico (Pardo & Suárez 1995; Pérez-Campos *et al.* 2008; Kim *et al.* 2010) and the steep subduction of northern Central America (Syracuse & Abers 2006). The seismicity indicates that the Wadati–Benioff zone transitions smoothly through the region, even as it crosses the boundary between the North American (NA) and Caribbean (CA) plates (Burbach *et al.* 1984; Rebollar *et al.* 1999). The slab dip varies from horizontal near Mexico City, 30° where it crosses the Isthmus of Tehuantepec, to 45° where it crosses the Mexico–Guatemalan border (Burbach *et al.* 1984; Rebollar *et al.* 1999, Fig. 1a).

The volcanic arc, however, does not follow this smooth transition (Fig. 1a). In central Mexico, the arc was active along the coast until it extinguished ∼25 Ma. During the early Miocene, the arc reappeared rapidly inland ∼250 km to the northern edge of the Trans Mexican Volcanic Belt (TMVB, Ferrari 2004). Slab rollback in the mid-to-late Miocene has brought it to its current location along the southern edge of the TMVB (Ferrari 2004). In Central America, southeast of the Mexico–Guatemala border, the active arc is along the coast where the Cocos Plate is at 100 km depth under the CA Plate. In between, in southeastern Mexico, the active arc is discontinuous, and consists of three isolated volcanic zones: Los Tuxtlas Volcanic Field (LTVF), El Chichión and the Modern Chiapanecan Volcanic Arc (MCVA). These zones do not have the usual location relative to the underlying slab. The volcanic arc is typically situated where the slab is ∼100 km deep (Wada & Wang 2009), and is also situated parallel to the trench. In southern Mexico, the volcanic arc

*Now at: Lamont-Doherty Earth Observatory, Columbia University, Palisades, NY 10964, USA.

is missing where the subducted Cocos slab is ∼100 km deep. Active volcanic arcs, MCVA and El Chichón, are obliquely situated far inland from the Middle America Trench (MAT), where the slab depth is ∼200 km (Manea & Manea 2006). The LTVF is at the northern portion of our seismic line, much closer to the Gulf of Mexico.

In 2007–2008, a 45-station broad-band Veracruz-Oaxaca (VEOX) seismic line was deployed in southeastern Mexico across the Isthmus of Tehuantepec to image the subduction zone. The receiver function (RF) results show an image of the northeast-dipping Cocos slab down to ∼120 km depth, but in addition, the RF image also shows a slab-like structure that dips 35° to the south that can be seen to 250 km depth. This anomalous feature has no known role in the current tectonic models of the region.

In this paper we show the RF results and present a model to support a hypothesis that the anomalous slab may have been due to the collision of the Yucatán Block with the rest of Mexico. The timing of this event is likely indicated by the Chiapas Fold and Thrust Belt (CFTB), which is a compressional structure parallel to the proposed suture zone and was created ∼13–11 Ma (Mandujano-Velazquez & Keppie 2009). Other authors have proposed that the Yucatán Block (including the Campeche shelf) should be reconstructed with its northwestern continental shelf edge adjacent to the southeastern continental shelf edge of North America in Triassic time (e.g. Bird *et al.* 2005; Dickinson 2009, and references therein), but have generally assumed its separation from the Gulf coast that occurred in the Jurassic. This is consistent with the standard model for the age of the deep seafloor in the Gulf of Mexico (Pindell & Dewey 1982; Marton & Buffler 1994). The model we are proposing would have the Yucatán Block rotate clockwise to a position near Florida during opening of the Gulf in the Jurassic, and then move southwestwards relative to North America to its current position during the Miocene.
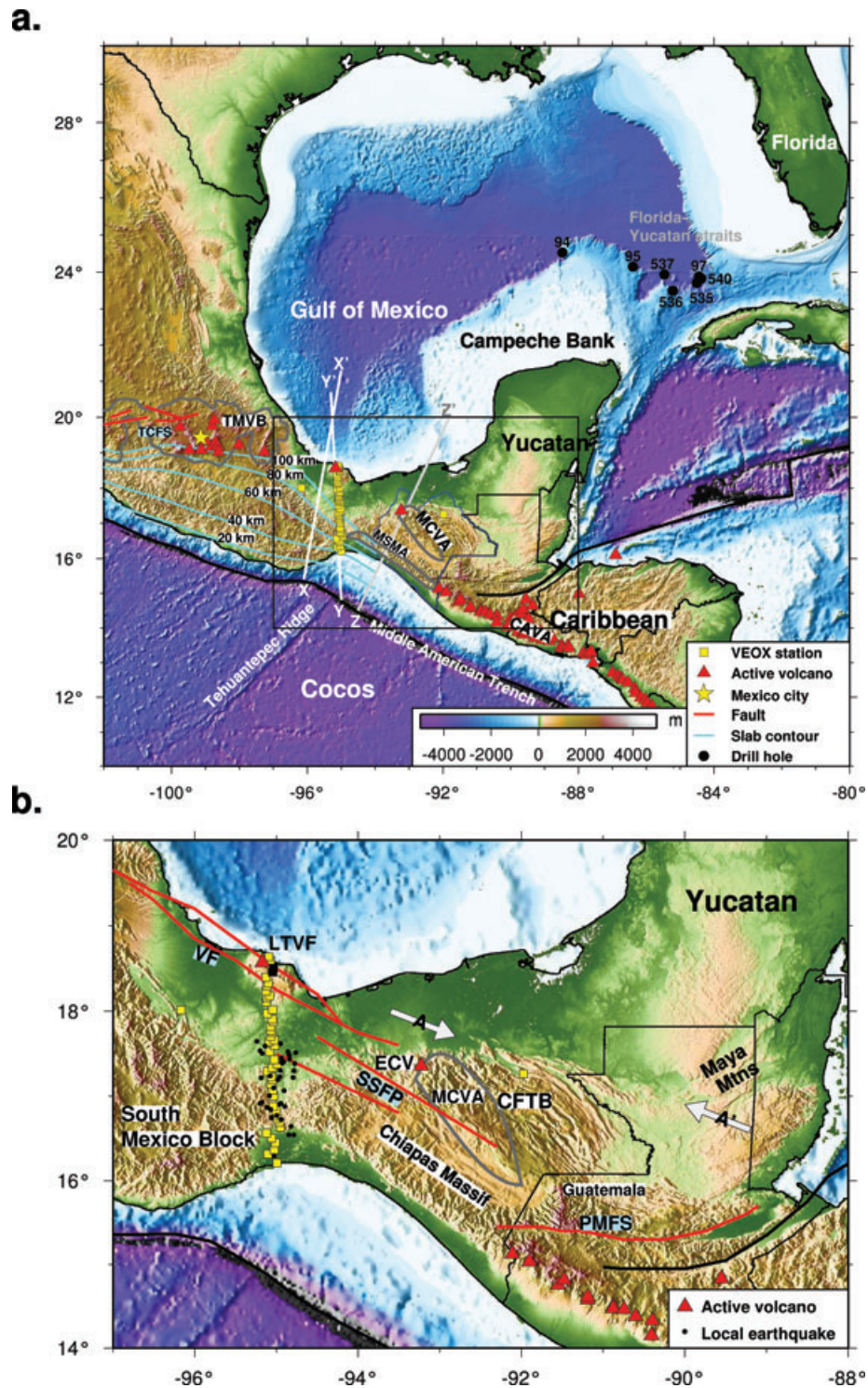
Figure 1. Topographic-bathymetric maps showing the region of the study and stations. (a) The map showing station locations of the VEOX seismic line in yellow squares and active volcanoes in red triangles. Isodepth contours of the Cocos Plate beneath the North American (NA) Plate (Pardo & Suárez 1995) are shown as cyan lines in the map. Locations of tomographic profiles are indicated as lines X-X′, Y-Y′ (along the VEOX line) and Z-Z′. Black dots with site numbers indicate selected Deep Sea Drilling Project (DSDP) drill holes. Grey solid lines represent volcanic belts (TMVB in central Mexico and MCVA in the Chiapas State). A blue solid line represents the Chiapas State. Red lines within the TMVB outline the TCFS, and their locations were extracted from Andreani *et al.* (2008). The abbreviations shown in the map are TMVB, Trans Mexican Volcanic Belt; MCVA, Modern Chiapanecan Volcanic Arc; MSMA, Miocene Sierra Madre Arc; CAVA, Central American Volcanic Arc; TCFS, Tula-Chapala Fault system. (b) Regional topographic map showing a lineament in the approximate location of the proposed Mexico–Yucatán suture zone, indicated by two grey arrows (A and A′). The selected local earthquakes, recorded from the VEOX line, are plotted as black dots near the VEOX line. Red lines outline main fault systems in southern Mexico, and their locations from Andreani *et al.* (2008). The abbreviations shown in the map are LTVF, Los Tuxtlas Volcanic Field; ECV, El Chichón; VF, Veracruz Fault; SSFP, Strike-Slip Fault Province; PMFS, Polochic-Motagua Fault System; CFTB, Chiapas Fold and Thrust Belt. The location of this map is shown in (a).

2 DATA AND RF IMAGING METHOD

We used teleseismic *P*-to-*S* (*Ps*) converted waves, also known as RFs (e.g. Vinnik 1977; Langston 1979), for imaging the lithospheric structure beneath southern Mexico. The method removes source-related and mantle-path effects by deconvolution, enhancing *Ps* conversions and reverberations associated with crustal and mantle

structure beneath the receiver. The amplitudes of the *Ps* phases primarily depend on the incidence angle of the impinging teleseismic *P* wave and the velocity contrast across the discontinuities. The relative arrival times of the converted phases and multiples depend on the depth of the velocity discontinuities, and the *P*- and *S*-wave velocity structure between the discontinuities and the surface (Zhu & Kanamori 2000).
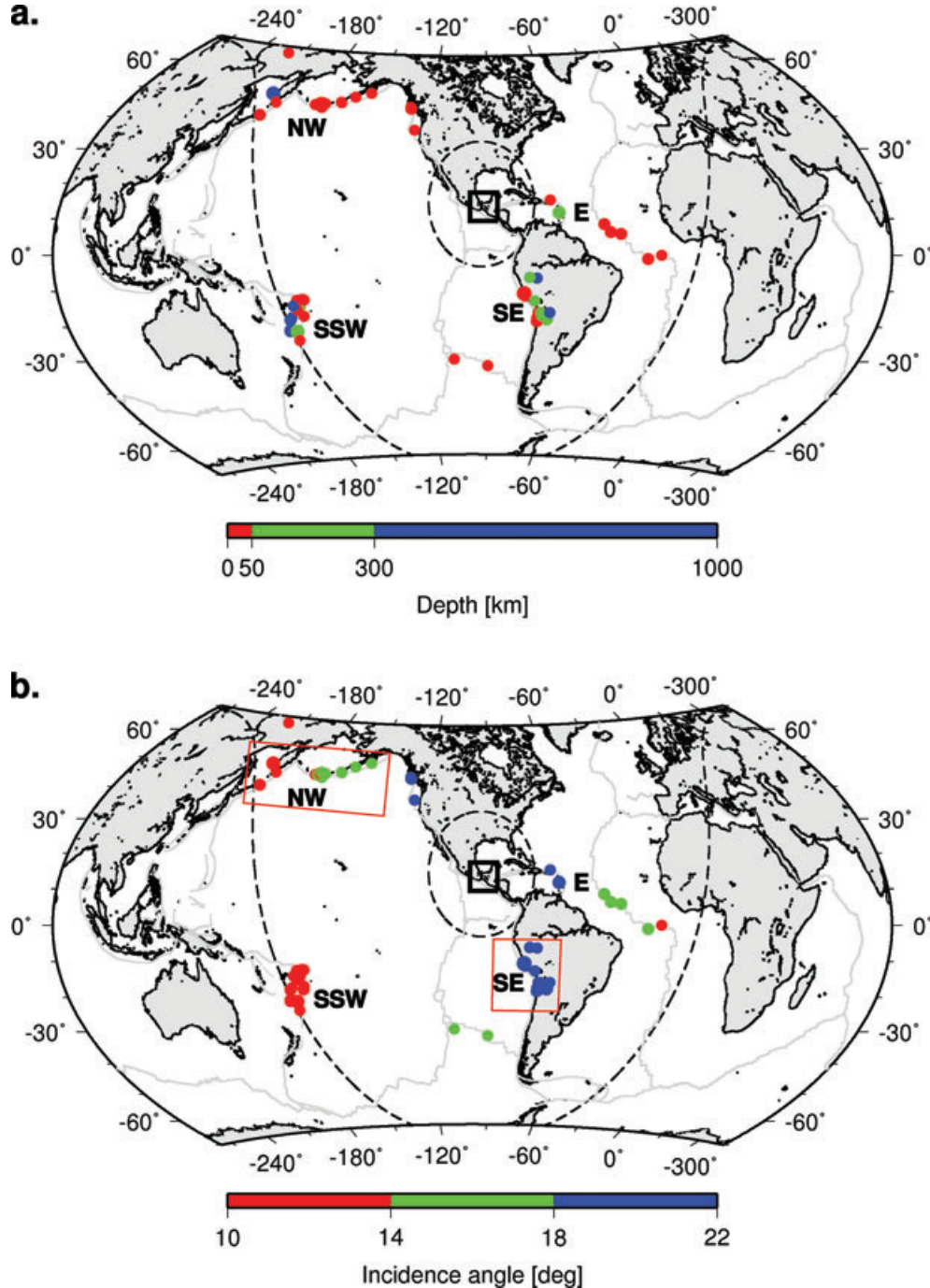

Figure 2. Distribution of teleseismic events used in the analysis, including 7 events in a east (E) backazimuth band from 82.5° to 97.1°, 20 events in a southeast (SE) band from 137.7° to 149.1°, 15 events in a south-southwest (SSW) band from 244.4° to 252.7°, and 23 events in a northwest (NW) band from 319.1° to 341.5° from the VEOX line enclosed in the box. Dashed lines are a distance of 30° and 90° away from the central point of the VEOX line. (a) Distribution of the teleseismic events coloured according to depths. The size of the circle is scaled to the size of the earthquake. (b) Distribution of the teleseismic events coloured according to the incidence angles of the teleseismic *P* waves impinging through the southwest-dipping slab from the Gulf of Mexico (Yucatán slab). The size of the circle is also scaled to the size of the earthquake. The events in SE and NW bands are enclosed in red boxes.

We will mainly concentrate on radial RFs, which can be obtained by deconvolving the vertical component seismograms from the radial components. Tangential RFs can also be calculated using the tangential component seismograms, and provide information on anisotropy and help to identify dipping structures (Savage 1998), but the tangential RF image (Fig. 4b) does not show strong conversions at the anomalous southwest-dipping slab from the Gulf of Mexico (see Section 3).

The location of the VEOX line is shown in Figs 1(a) and (b). The average distance between stations is about 6 km. Of 45 stations installed in southern Mexico, only 40 provided useable seismic records. For the RF analysis, a total of 68 teleseismic earthquakes of magnitude greater than 6.1 from 2007 July to 2008 October 2008, with epicentral distances between 30° and 90° and depth ranges between 6 km and 635 km, were used (Fig. 2a). The range in incident angles of the impinging P wave at the top of the anomalous southwest-dipping slab is illustrated in Fig. 2(b) Individual waveform data are time windowed to 90 s and rotated to radial and tangential coordinates. These data were then processed in two passbands, (1) a lower frequency band from 0.08 to 0.33 Hz and (2) a higher frequency band from 0.01 to 1 Hz.

We used the lower frequency band (0.08–0.33 Hz) to constrain the geometry of the Cocos slab based on the radial RFs. This band is used to improve the signal-to-noise ratio for stations near the Pacific coast, which were affected by frequent flooding, and to minimize the effect of local seismicity. We then used iterative time domain deconvolution technique (Kikuchi & Kanamori 1982; Ligorría & Ammon 1999) to compute the RFs, which worked better than frequency domain deconvolution (Langston 1979; Ammon *et al.* 1990) for imaging the slab. As shown in Fig. 2(a), the earthquakes generally occurred in four different backazimuth groups. The RFs from

each group is separately stacked to investigate the azimuthal variations. The higher frequency band (0.01–1.0 Hz) was used for the 20 events from the southeast (SE) backazimuth group to analyse the southwest-dipping slab.

In Fig. 3, the RFs used in the analysis are shown, sorted first by station position along the array, and second for each station, by backazimuth of the incident wavefields. Each column for a single station is separated by the vertical line from adjacent station. The distance between centre points of two adjacent columns represents the distance between two stations. The thickness of the RF column bin is thus not uniform for each station. The red and blue colours of the RF amplitudes in Fig. 3 correspond to velocity increase and decrease with depth, respectively. The colour of the images for radial and tangential RFs represents the absolute amplitudes of RFs.

3 SLAB IMAGE IN SOUTHERN MEXICO

Figs 4(a)–(d) show an image of the Cocos slab to a depth of about 120 km, along with the continental Moho of the overriding NA Plate between 3 and 5 s after the P-wave arrival at 0 s. The images are constructed incorporating the teleseismic events from all azimuths (Fig. 2), filtered to 0.08–0.33 Hz to increase the signal-to-noise ratio. The top and bottom interfaces of the oceanic crust of the Cocos slab are defined by the negative (blue) and positive (red) radial RF pulses, respectively (Fig. 4a). Oppositely polarized Ps pulses are the result of waves converted from the top and bottom boundaries of a dipping, low-velocity layer, indicated by dashed lines (Fig. 4c). A similar RF image of the Cocos slab can be found from Melgar (2009) and Melgar & Pérez-Campos (2010) using the teleseismic data filtered in the same low-pass band. The dip of the Cocos slab is estimated to be 25°. The consistent negative
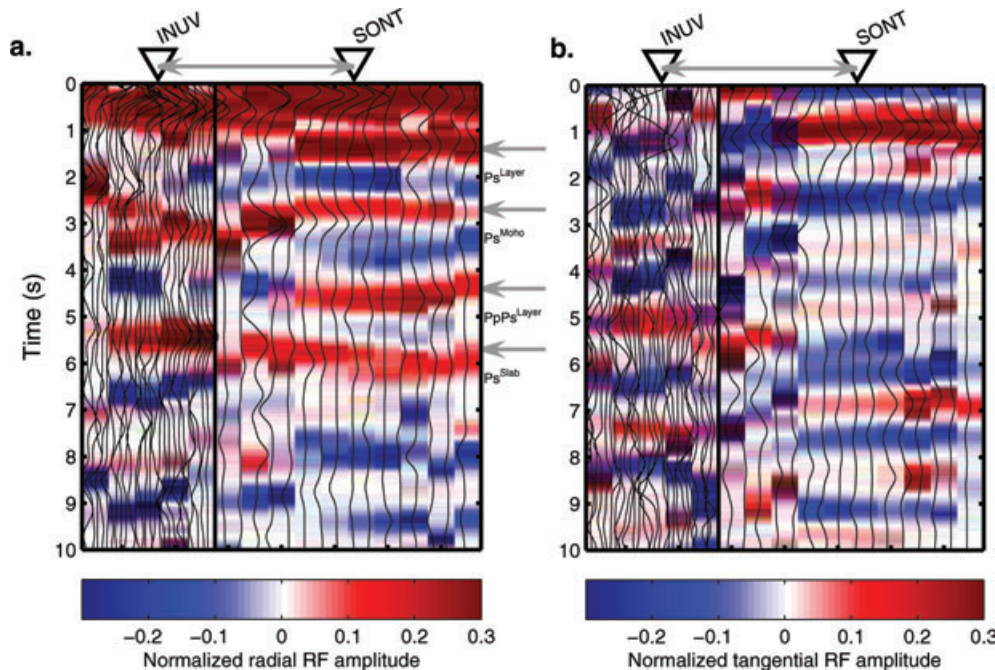

Figure 3. High-pass version of RF record section and RF image for two stations (INUV and SONT). The locations of the two adjacent stations are indicated as black squares at the northern part of VEOX line in Fig. 1(b). The figure demonstrates how the RF imaging is done. The RFs for each station are sorted by the order of increasing backazimuth of the incident wavefield. (a) The radial RF image overlain with 29 and 16 RF traces for stations INUV and SONT, respectively. A strong positive arrival between 4 and 5 s in SSW and NW bands is the seismic multiple phase (*PpPs*) from *Ps* phase between 1 and 1.5 s after P arrival at 0 s. Double pulses for the P arrival are commonly observed in the northern part of VEOX line, especially in the LTVF. Zamora-Camacho *et al.* (2010) also observed a layer at 10–14 km from the RF analysis, which they interpreted as the layer between the upper sedimentary layer and transitional crust found elsewhere in the margins of the Gulf of Mexico. (b) The tangential RF image overlain with 29 and 16 traces for stations INUV and SONT, respectively.
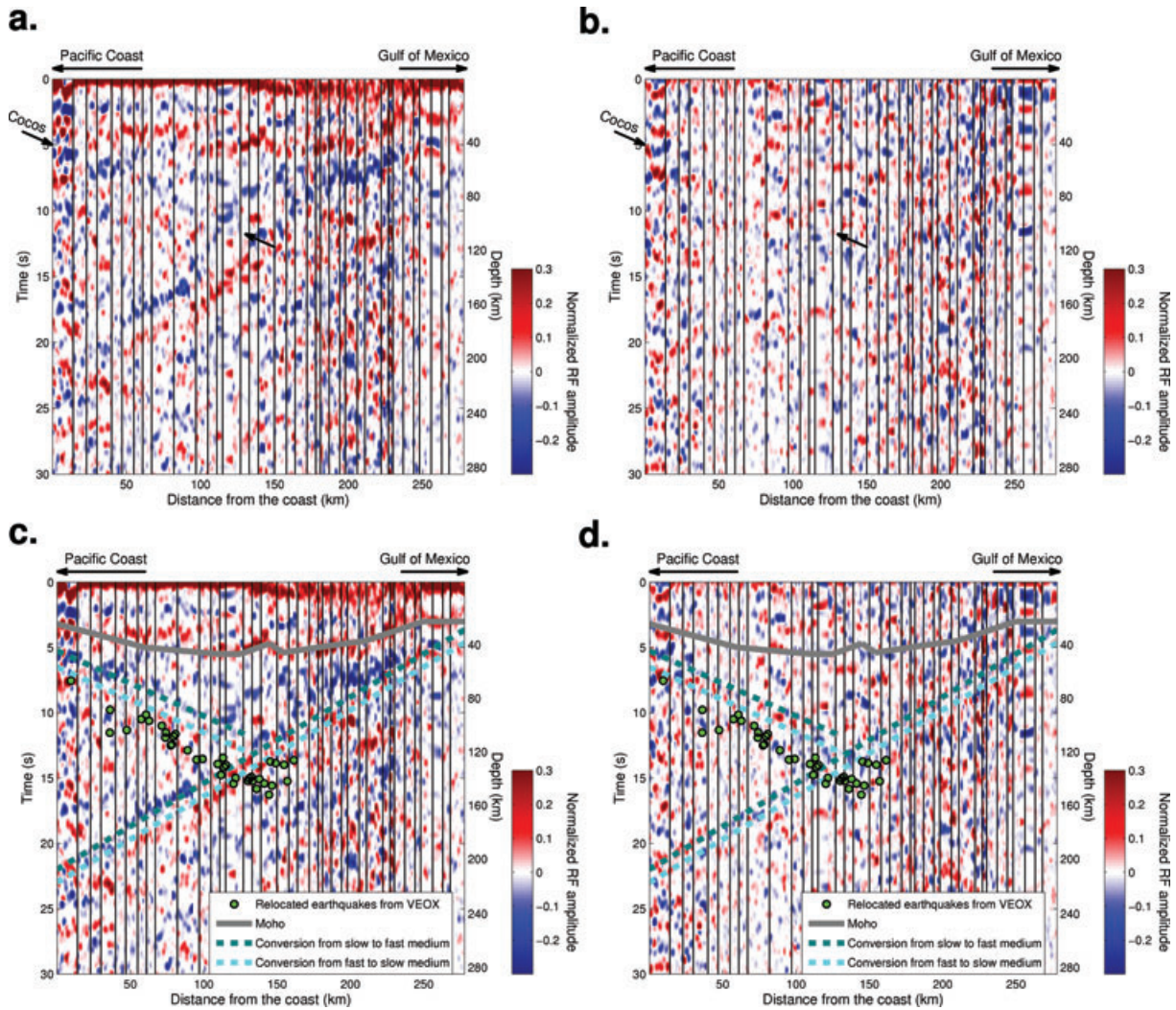
Figure 4. Low-pass version of the radial (a, c) and tangential (b, d) RF images showing Cocos slab, utilizing data from all azimuths (Fig. 2a). The seismograms from the 68 teleseismic earthquakes are filtered to 0.08–0.33 Hz. The time axis on the left-hand side is mapped directly to the depth on the right-hand side using IASP91 velocity model (Kennett & Engdahl 1991). (a) The radial RF image without interpretation lines. (b) The tangential RF image without interpretation lines. (c) The radial RF image showing Cocos slab with local seismicity. The top and bottom interfaces of the Cocos oceanic crust are indicated by dotted lines, and separated by 8–10 km thickness. The local earthquakes plotted are recorded from the VEOX line as green circles. The 38 earthquakes from the VEOX line are relocated using the double-difference algorithm of Waldhauser & Ellsworth (2000) (Castro Artola 2010). The earthquakes are selected from epicentres within 25 km of the VEOX line (Fig. 1b). (d) The tangential RF image with interpretation lines and local seismicity.

RF pulse before the positive RF pulse indicates an existence of the low-velocity layer at the top part of the subducting oceanic crust, which is discussed in detail in Kim *et al.* (2010). The most probable cause of the breakdown in the negative arrival trend is suggested to be completion of gabbro to eclogite transformation (Yuan *et al.* 2000; Jacobsen & van der Lee 2006; Kawakatsu & Watada 2007), and in southern Mexico we speculate that the eclogitization has not occurred yet based on the clear negative impedance contrast at the top of the oceanic crust. The location of the Cocos oceanic crust can be also traced in the tangential RF image (Figs 4b and d) although the tangential RF amplitudes are a factor of 2 smaller than the radial ones.

The local seismicity in Figs 4(c) and (d) delineates a Wadati–Benioff subduction zone beneath the continental Moho. A total of 38 local earthquakes in the magnitude range from 3.4 to 5.7 occurred along the VEOX line from 2007 September to 2009 March. These events were relocated using data from the VEOX array and the *S*-wave velocity model of Campillo *et al.* (1996), derived

from the inversion of group velocity dispersion data (Castro Artola 2010). The double-difference algorithm of Waldhauser & Ellsworth (2000) was used leading to an estimated depth error of 2–4 km. As shown in Figs 4(c) and (d), most of the seismicity occurs below the oceanic crust and within the oceanic mantle of the subducted Cocos slab. We note that small difference in slope between the relocated seismicity and converted *Ps* phases corresponding to the oceanic crust is primarily from the difference in the velocity model used. The main difference comes from the crustal velocities from 0 to 17 km, which will lead to up to a 3.07 s delay in phase arrival times.

The image shown in Fig. 5(a) is the stack of 20 events that span a distance range of 40°–50° with source depths ranging from 20 to 635 km (Fig. 5a). In this figure, there is a clear southwest-dipping structure (denoted hereafter as the Yucatán slab) that extends from the northernmost station on the Gulf of Mexico to 250 km depth with a 35° dip. This image is constructed incorporating teleseismic events from the SE backazimuth band (Fig. 2a), filtered to 0.01–1 Hz. The Yucatán slab appears to truncate the Cocos slab image at ∼120 km
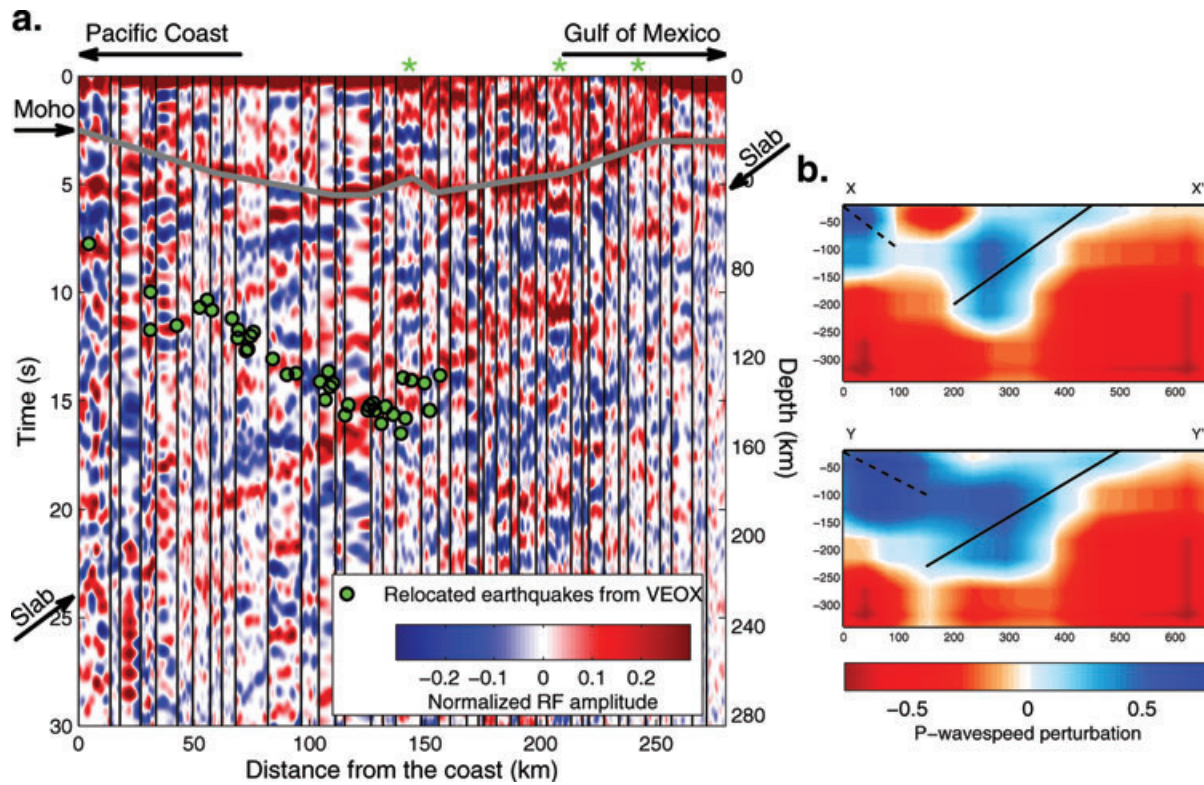
Figure 5. High-pass version of RF and global tomography results. (a) RF image showing the Moho and the Yucatán slab from the Gulf of Mexico. The seismograms from the 20 teleseismic earthquakes are filtered to 0.01–1 Hz. The locations of teleseismic earthquakes used to construct the RF image are shown in Fig. 2(b) (red box, labelled as SE). The local earthquakes plotted are the same ones in Figs 4(c) and (d). The receiver gathers for stations indicated as green asterisk symbols are in Fig. 6. (b) Cross-sections of the profile X-X′ and Y-Y′ (Fig. 1a) through the global *P*-wave tomography model of Li *et al.* (2008), showing the image of the Yucatán slab (solid lines) and Cocos slab (dotted lines).

depth (Fig. 5a). We note that the Cocos slab is only weakly visible in this image because the higher frequency filter is used. There is some indication that the seismicity follows the trend of the Yucatán slab starting at the intersection point with the Cocos slab (Figs 4c and 5a). A similar focused zone of earthquakes ('the Bucaramanga nest') was also found where the Caribbean and Nazca Plates collide under Colombia (Zarifi *et al.* 2007).

The image of the Yucatán slab is sharp and well defined for its entire length, except for its termination at depth, which is somewhat ambiguous (Fig. 5a). Examples of receiver gathers for three stations in the middle and northern section of the VEOX line show clear arrivals from the slab structure only in the SE backazimuth range (Fig. 6). This indicates that the Yucatán slab exists primarily to the east of the VEOX line. This result is also supported by the global tomography result (see Section 5). We note that the Yucatán slab is also observed in the low-passed RFs in Fig. 4(a), but it is somewhat fuzzy because events from all backazimuths are included in the RF stack.

The image of the Yucatán slab is unlikely to be an artefact because the various ray paths (Fig. 2) that are used to construct the image are sufficiently different, and are also far enough away from the triplications in the upper mantle. Thus, it is unlikely that source-side structure and path effects are mapped into the image. Scattering from near-surface structures adjacent to the VEOX line would tend to produce weak incoherent arrivals and not the strong linear image that is seen in Fig. 5(a). A linear feature could be produced by scattering of surface waves by an unknown shallow feature at the northern end of the VEOX line, but if this were the case, the observed phase velocity would be ∼9 km s^{-1}. The RF image using the

transverse component does not show a strong image of the Yucatán slab (Fig. 4b), indicating that the cross-dip and anisotropy effects are minimal.

4 RF FINITE-DIFFERENCE MODELLING

To further investigate the RF images that show the Cocos and Yucatán slabs, we produce synthetic RFs with a 2-D finite-difference wave propagation program for particular velocity and slab geometry models and compare these to the data. The laterally complicated structure, such as two opposing slabs (Cocos and Yucatán slabs) and Moho, leads to very complicated images containing converted phases, *P*d*s* (*P*-to-*S* conversion at a discontinuity, d) and *P*m*s* (*P*-to-*S* conversion at the Moho, m), and their seismic multiples. To focus on the subducted slabs, we construct two simple models that only include the Cocos slab (Model 1, Fig. 7a) or the Yucatán slab (Model 2, Fig. 8a) to avoid seismic multiples in the synthetics, which interfere with direct arrivals from the Cocos and Yucatán slabs. The seismic multiples in the data are in fact very weak as they are on the Meso America Subduction Experiment (MASE) to the northwest (Kim *et al.* 2010). To include a crust in the finite-difference model, the modelled interface needs to be randomized on a fine scale or scaters need to be included in the crust to attenuate the multiples. Thus, we only show the RF synthetics generated from the two simple models (Figs 7a and 8a) and investigate how the synthetics behave with different frequency filters (1, 2 and 3 s) and the incidence angle of the incoming plane waves (SE or NW). We show the RF synthetics generated from a velocity model, which
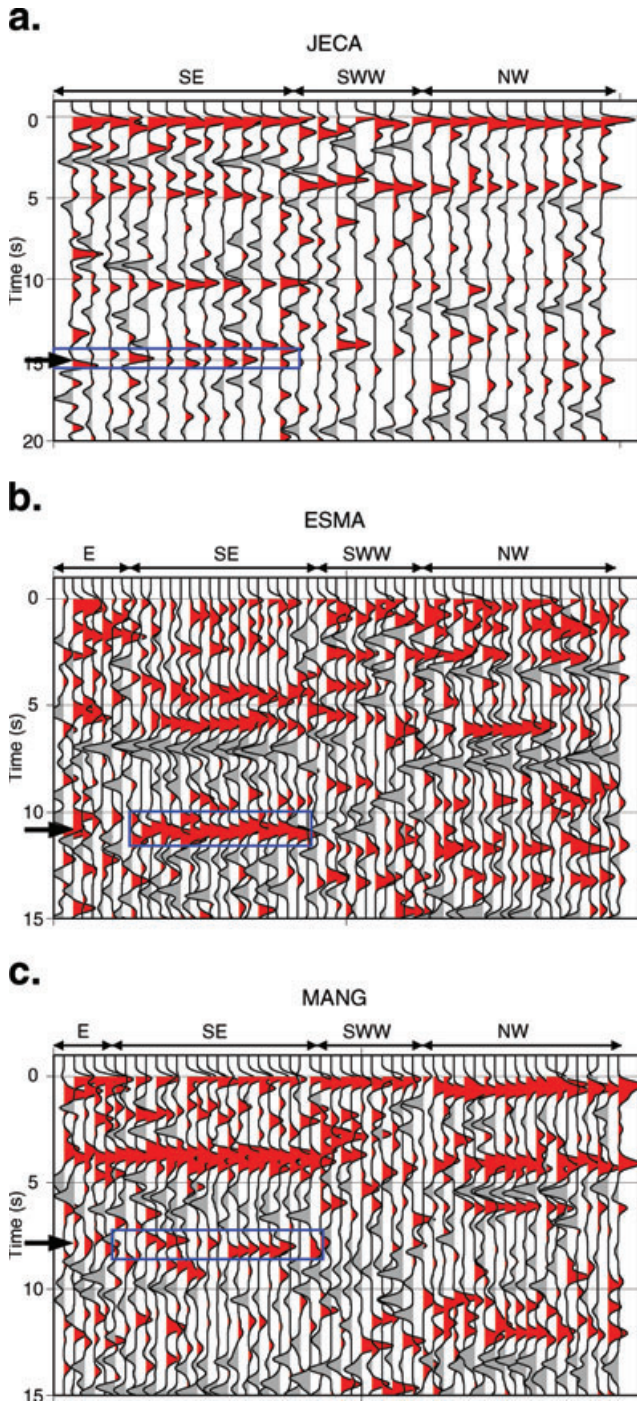
Figure 6. RF gathers from three stations (JECA, MANG and ESMA) that show the arrival (in a blue box) from the Yucatán slab only on the SE backazimuths. Each seismogram is filtered to 0.01–1 Hz. Locations of the stations are shown in Fig. 5(a), and the stations from top to bottom are in the order of increasing distance from the Pacific coast.

fits the amplitude of the negative and positive pulses corresponding to the top and bottom of the subducting crusts, respectively, and the timing of these two pulses.

For the Cocos oceanic crust in southern Mexico, we use same velocities (but slightly different thickness for the upper and lower oceanic crusts) obtained for central Mexico (Kim *et al.* 2010). In southern Mexico, we observe strong conversion at the top of the oceanic crust (see data traces plotted in Fig. 7b), which indicates

very slow velocities at the upper oceanic crust. Kim *et al.* (2010) divided the subducted Cocos oceanic crust in central Mexico into two layers to achieve a comparable velocity contrast at the top and bottom interfaces of the oceanic crust that they observed from the 1 s RF data. Based on the RF finite-difference modelling, Kim *et al.* (2010) reported anomalously low shear speeds at the upper oceanic crust (2.4–3.4 km s^{-1}) with its thickness of ∼4 km at ∼20–40 km depth. Such slow velocities at the upper oceanic crust may indicate the presence of water and hydrous minerals or high pore pressure (Kim *et al.* 2010). On the other hand, we observe weak negative conversion at the top of the subducted Yucatán slab (see data traces plotted in Fig. 8b), and two converted pulses at the top and bottom of the subducted crust are more separated in time.

Fig. 2(b) shows calculated incident angles at the top of the Yucatán slab, which range from 18° to 22° for the SE quadrant and from 10° to 18° for the NW quadrant. For the typical RF synthetics, plane waves with variable incident angles in the range of the ray parameter from 0.04 to 0.08 (18.66° to 39.79°) are used. In our analysis, since the incoming angle is quite small (10° to 22°), we only generate the synthetic seismograms using the ray parameter of 0.04 (18.66°). In addition, we use the iterative time domain deconvolution (Kikuchi & Kanamori 1982; Ligorria & Ammon 1999) to convert the synthetic seismograms to the radial RFs (Figs 7b and 8b).

We first note that the amplitudes of the synthetic RFs for the SE and NW quadrants are different for all three frequency bands (Figs 7b and 8b). The amplitudes of the converted waves from both slabs are more sensitive to the direction of the incoming wave. In Fig. 8(b), the amplitudes of the synthetic RFs for the NW quadrant are consistently smaller than those for the SE quadrant for the Yucatán slab. We do not see such a significant reduction in amplitude for the Cocos slab (Fig. 7b). This simulation result may explain why we do not see strong conversions from the Yucatán slab in the NW backazimuth in the real data (Figs 5a and 6), and also why this dipping feature becomes degraded if all the azimuth data are added in the image (Fig. 4a).

5 TOMOGRAPHIC IMAGES

Many cross-sections through Mexico from global *P*-wave tomographic inversions have shown a coarse-scale image of the Cocos slab (Rogers *et al.* 2002; Gorbatov & Fukao 2005; Li *et al.* 2008). In Fig. 5(b), two slices from a tomographic *P*-wave model of Li *et al.* (2008) show a southward-dipping structure (in blue colour, representing fast *P*-wave perturbations) similar in dip and length to the one seen in the RF image (Fig. 6a). This dipping structure is not present in the northern part of the MASE from the tomography model and previous RF studies in central Mexico (Pérez-Campos *et al.* 2008; Kim *et al.* 2010). The grid size that Li *et al.* (2008) used in the tomographic inversion is approximately 0.7° in latitude and longitude and 45 km in depth. The resolution of the tomographic models is poor at this scale, but they do confirm the existence of the Yucatán slab and that it continues farther to the southeast of the VEOX line (Fig. 9b). In addition, the recent tomographic images of *P*- and *S*-wave velocities derived from local earthquakes recorded by the VEOX line (Chen & Clayton 2010) also show the Cocos and Yucatán slabs, although their images are limited to 100 km in depth due to the maximum depth range of the local earthquakes.

The model by Li *et al.* (2008) also shows that the Cocos slab appears to have broken with the detached portion having descended to about 300 km depth (Fig. 9b). This evidence of slab truncation
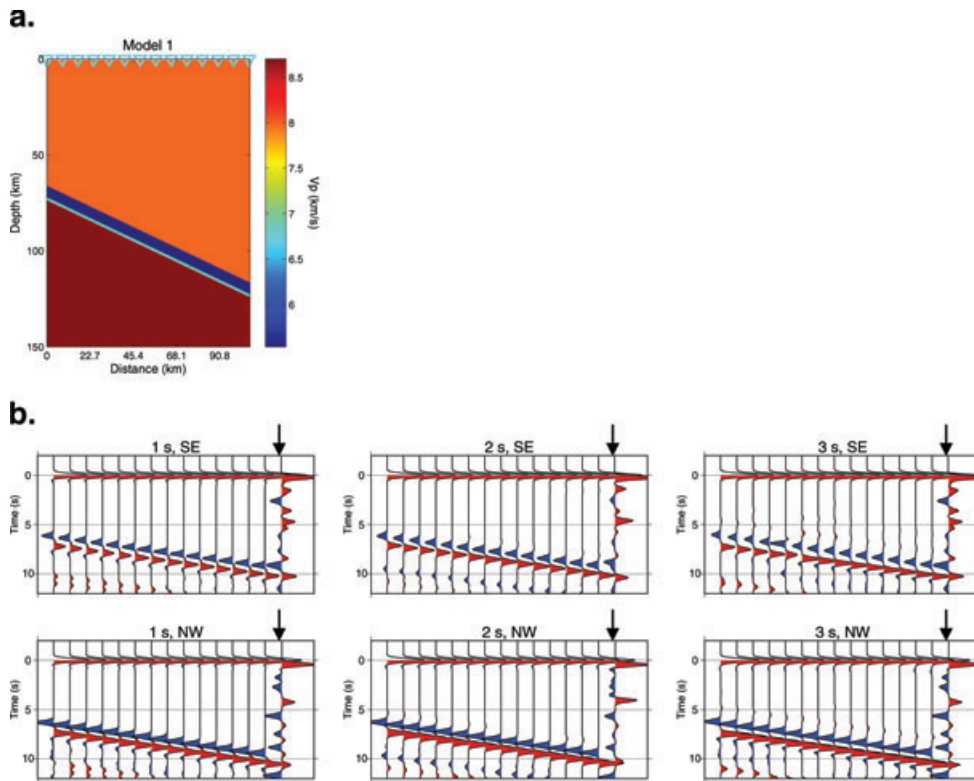
Figure 7. RF finite-difference modelling result for the Cocos slab. (a) Geometry of the model, including the Cocos slab with a dip of 25°. We inserted a slab based on Kim *et al.* (2010), that includes a very low *S*-wave velocity on top. We note that the estimate of the thickness of the low-velocity layers for the oceanic crust slightly trades off with their velocities. The colour represents the *P*-wave velocity in km s^{-1}. (b) The 1 s, 2 s and 3 s synthetics with two different directions of incoming plane waves (SE or NW) are shown. The red and blue colours represent the positive and negative impedance contrasts, respectively. The data trace included in each record section is indicated by the arrow.

along with profiles farther to the southeast was used by Rogers *et al.* (2002) to argue that the uplift of the highlands in Honduras is due to the inflow of the asthenosphere resulting from the breaking of the slab. Using hypsometry of the uplift in Honduras, the slab detachment is estimated to be ∼10–5 Ma (Rogers *et al.* 2002). The gap in the slab provides an avenue for the Yucatán slab to cross the Cocos slab, and may indicate that the Yucatán slab is responsible for the truncation.

6 TECTONIC AND VOLCANIC FEATURES

There are a number of interesting and anomalous tectonic features in southern Mexico that are assumed to be a result of subduction, but are not well explained by a simple model of the Cocos Plate subducting under the NA Plate. The Isthmus of Tehuantepec is an anomalous topographic low above the Cocos subduction zone (Fig. 1b). To the east, the CFTB is a compressive structure with ∼106 km of minimum shortening that occurred between ∼13 and ∼11 Ma (Mandujano-Velazquez & Keppie 2009). The terranes on either side of the CFTB are different (to the southwest is the Permian Chiapas Massif, to the northeast is the Mesozoic/Cenozoic stratigraphy deformed in the CFTB). Both this topographic low and the CFTB shortening have been expected by subduction of the Tehuantepec Ridge (TR) asperity on the Cocos Plate (Manea *et al.* 2005; Mandujano-Velazquez & Keppie 2009). The CFTB is confined to the southern Mexican interior northeast of the Chiapas massif, and the deformation trace may continue eastwards into

Guatemala (Fig. 1b). These features of the CFTB do not appear to be caused by subduction of the TR.

In Fig. 1(a), the currently active volcanoes in the region are shown. In central Mexico, the active arc is along the southern edge of the TMVB where the slab is at ∼100 km depth. In the south, the Central American Volcanic Arc (CAVA, Fig. 2a) is along the coast, where the slab is also at 100 km depth. In between, the Modern Chiapanecan Volcanic Arc (MCVA, Fig. 2a) is at a strike of ∼30° clockwise from the strike of the MAT and lies ∼200 km above the Cocos slab (Manea & Manea 2008). In this region the Cocos slab, as delineated by seismicity (Rebollar *et al.* 1999), ranges in dip from 50° to 54°, which is not sufficient to explain the MCVA's oblique strike angle. The volcanoes become progressively older to the south-southeast with initial dates ranging from 1.3 to 3 Ma (Mora *et al.* 2007), which indicates the system is evolving.

The Miocene Sierra Madre arc (Fig. 1a) lies along the coast and extinguished at approximately 9–3 Ma (Damon & Montesinos 1978). A model by Manea & Manea (2008) to explain the MCVA and the extinct Miocene Sierra Madre arc along the coast proposes that the influx of hot mantle wedge material from slab flattening event in central Mexico at 29–19 Ma is the source for the modern volcanism, while the cold (flattened) slab shuts off the Miocene Sierra Madre arc. In the northern part of the Tehuantepec Isthmus, the LTVF is ∼7–0 Ma in age and alkaline by affinity (Verma 2006). If the Cocos slab is projected beneath the LTVF, it would lie ∼250 km beneath the LTVF, or deeper if the slab truncation models are correct (Rogers *et al.* 2002).

El Chichón lies between the MCVA and the LTVF, and is a very young (0.2 Myr) isolated adakite volcano, that may be related to the
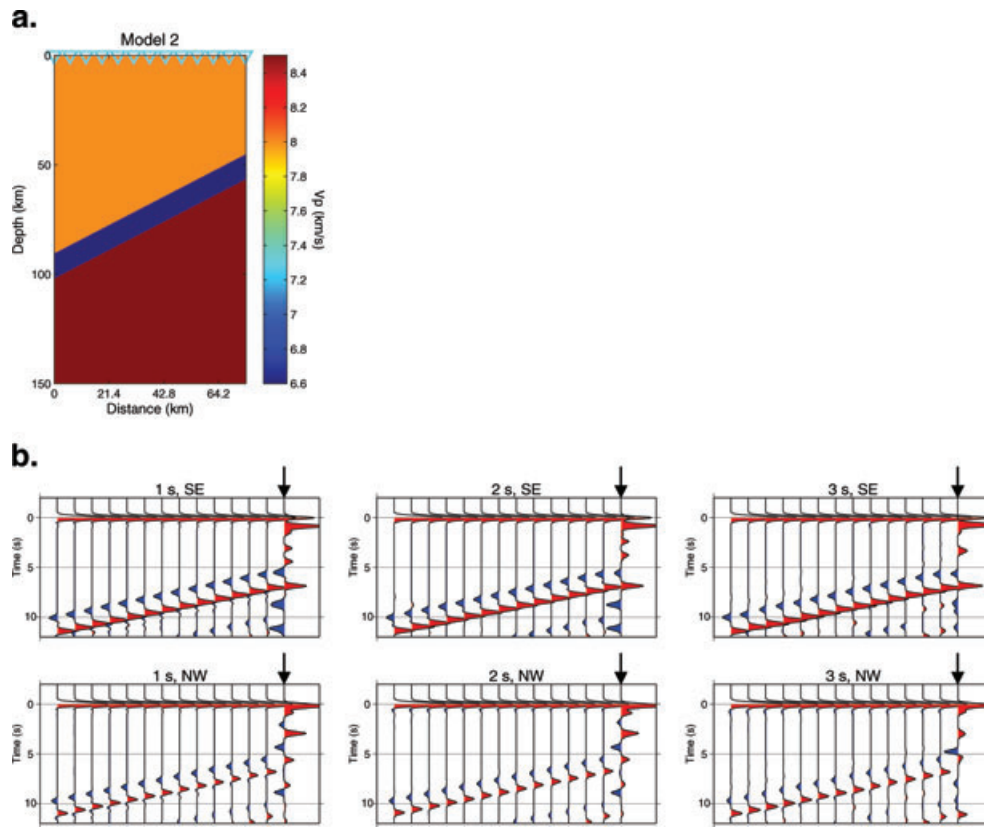
Figure 8. RF finite-difference modelling result for the Yucatán slab. (a) Geometry of the model, including the Yucatán slab with a dip of 35°. The colour represents the *P*-wave velocity in km s^{-1}. (b) RF synthetics from the model shown in (a). The 1 s, 2 s and 3 s synthetics with two different directions of incoming plane waves (SE or NW) are shown. The red and blue colours represent the positive and negative impedance contrasts, respectively. The data trace included in each record section is indicated by the arrow. Note that the ∼50 per cent reduction in the converted amplitudes at the top interface of the subducted Yucatán slab in the NW swath compared to ones in the SE swath.

subduction of the TR (Manea & Manea 2008). The MCVA, LTVF and El Chichón volcanism do not appear to be the result of normal Cocos slab dehydration because slab depths are 200 km or deeper below the volcanic centres.

7 DISCUSSION

Previous models of Yucatán Block motion and Gulf of Mexico opening since the breakup of Pangea in the Mesozoic seem to provide no explanation for the Yucatán slab structure. Most models suggest that the Yucatán Block rotated in counter-clockwise fashion away from the northern Gulf of Mexico margin during the Jurassic (Pindell & Kennan 2009, block trajectory is shown in Fig. 10b). Dextral shear zones in eastern Mexico/western Gulf of Mexico accommodated this motion. This motion is compatible with some interpretations of magnetic anomalies in the deep Gulf of Mexico basin (Hall & Najmuddin 1994), possible hotspot tracks in the deep Gulf of Mexico basin (Bird *et al.* 2005), and preferred positions of the Yucatán Block in Pangean reconstructions (e.g. Dickinson 2009). This interpretation would not be compatible with the Yucatán slab because it does not predict convergence between the Yucatán and the South Mexico Blocks. Also, if the Yucatán slab structure formed during the Jurassic, it seems unlikely that such an old inactive structure would have sufficient buoyancy to remain as shown in Fig. 6(a), and it should have descended into the deeper mantle long ago (Billen 2008).

Our preferred hypothesis is that the Yucatán slab represents seafloor subducted prior to a collision of the Yucatán Block with southeastern Mexico (Fig. 10a). Strictly speaking, neither the timing of the proposed collision nor the relative motion of the Yucatán and South Mexico Blocks are constrained by the Yucatán slab structure. However, we speculate on a possible evolutionary model as follows. To accommodate this hypothesis and the Jurassic age of the Gulf of Mexico basin, we suggest that the historical motion of the Yucatán Block took place in two stages. During the opening of the Gulf, a first Jurassic stage involves a clockwise rotation of the Yucatán Block away from the northern Gulf of Mexico coast (Fig. 10b). The key difference is that we propose this stage finishes with the Yucatán Block placed off the southwest coast of Florida. Then, a second stage, in the Miocene, would involve the southwest migration of the Yucatán Block (<250 km, i.e. up to the inferred length of the Yucatán slab) into its current position (Fig. 10). The late stage would finish with the collision of the Yucatán Block against southeast Mexico and provides an explanation for the formation of the CFTB in southeast Mexico.

In this model, the ∼13–11 Ma age of deformation in the CFTB constrains the timing of continental collision. The model in Fig. 9(a) shows the place where the proposed suture zone intersects the surface within the Mesozoic/Cenozoic stratigraphy along the northward projection of the VEOX line. The most prominent lineament to the southeast of this point is the northern edge of the CFTB, marked by the grey A-A′ arrows in Fig. 1(b). There is a clear lineament in the approximate location where we predict the suture
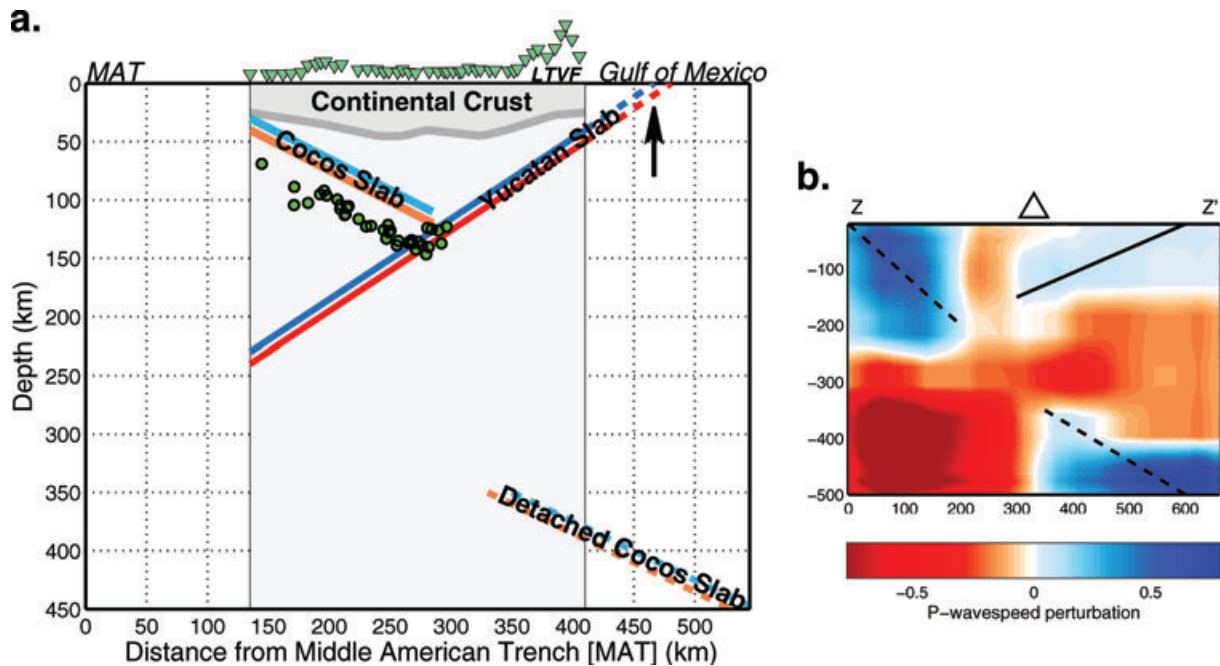
Figure 9. The model showing the structures constrained by the RF and tomography results. (a) The composite model showing the structures along the VEOX line, based on the RFs and global tomographic image by Li *et al.* (2008). The structures down to a depth of 250 km are constrained by the RFs, and the location of the detached slab is from the global *P*-wave tomographic image. The local earthquakes plotted as green circles are the same ones in Figs 4(c and d) and 5(a). The black arrow indicates the location of the proposed suture zone. The green inverted triangles show stations indicating relative elevations. (b) Cross-section image of the profile Z-Z′ (Fig. 1a) through the tomography model of Li *et al.* (2008). The Cocos slab is indicated by dotted lines, and the Yucatán slab by the solid line. The profile crosses the active El Chichón volcano (triangle symbol).

zone should be. It is terminated on its eastern end by the Northern Boundary Fault of the Maya Mountains (Fig. 1b).

We note that there is no palaeomagnetic data from the northeast Maya Block to constrain a model. Most of the palaeomagnetic data comes from within the Chiapas Massif, within the CFTB, or within the Maya Mountains, which are all south of our proposed suture zone. The best palaeomagnetic data for rocks within the CFTB is presented in Guerrero *et al.* (1990). These data give a palaeopole for the CFTB in roughly its present position relative to the NA Plate for *ca.* 150 Ma. Since the CFTB is part of South Mexico Block, the palaeopole that shows no movement relative to NA Plate does not affect our case.

The South Mexico Block appears to have been moving southeastwards relative to the main NA Plate, since the Miocene (Andreani *et al.* 2008). This has been accommodated by sinistral transtension in the Tula-Chapala Fault system (TCFS), roughly parallel to the TMVB (Andreani *et al.* 2008, Fig. 1a). Southeastward migration of the South Mexico Block may have initiated shortening at its eastern margin. Progressive shortening between the South Mexico and Yucatán Blocks may have evolved into a self-sustaining southwest-dipping subduction zone, which would account for the inferred southwestward migration of the Yucatán Block. We prefer a model that incorporates relative southwestward migration of the Yucatán Block, because we hypothesize that evidence for sufficient extension in the deep water Florida–Yucatán straits is more likely to be found than evidence for sufficient sinistral slip in the TCFS. Our model predicts early- to mid-Miocene extension in the Florida-Yucatán straits between Florida and the Campeche Bank (Fig. 1a), prior to the formation of the CFTB.

The idea of the Yucatán once being connected to Florida is support by the 30–50 s Rayleigh-wave phase-velocity maps which show

that Yucatán and Florida have a velocity that is distinctly faster than the rest of Mexico or the western Gulf region (Gaite *et al.* 2010). In addition, bathyal sediments of Cretaceous age observed in drill core from the Deep Sea Drilling Project (DSDP) holes 10-94, 10-95, 10-97, 77-535, 77-536, 77-537 and 77-540 (Fig. 1) have been interpreted to indicate a stable basin within the Florida–Yucatán straits throughout the Cenozoic (Worzel 1973; Buffler *et al.* 1984). On the other hand, missing intervals of Cenozoic section in these cores indicate significant slumping and mass wasting has occurred since the Miocene. The slumping and mass wasting could simply be due to gravitational instabilities, but may also be compatible with the tectonic extension predicted in our model. The extension does not appear to involve spreading along a ridge, and in this respect it may be similar to the extension that is currently occurring in the northern Gulf of California (Gonzalez-Fernandez *et al.* 2005). The opening of a deep water channel between the Yucatán Block and Florida may also explain the initiation of the oceanic Loop Current in the eastern Gulf of Mexico in the mid-Miocene (Mullins *et al.* 1987).

The dynamics of the slab subduction appear to be quite unusual in this region. The Yucatán slab appears to cut-off the Cocos slab at ~120 km depth (Fig. 9a) thus stopping standard 2-D mantle–wedge flow for both systems. It is almost certain that the 3-D flow is important in this region, and this may explain the unusual configuration of the arc volcanism in southern Mexico. A poorly understood mechanism involving competition between the Cocos slab and the Yucatán slab may be related to the proposed detachment of the Cocos slab at ~10–5 Ma (Rogers *et al.* 2002). The truncation of the Cocos slab would need to have occurred near the Pacific ocean trench to put the leading edge of the present Cocos slab at a depth of about 120 km as interpreted in Fig. 4(a).
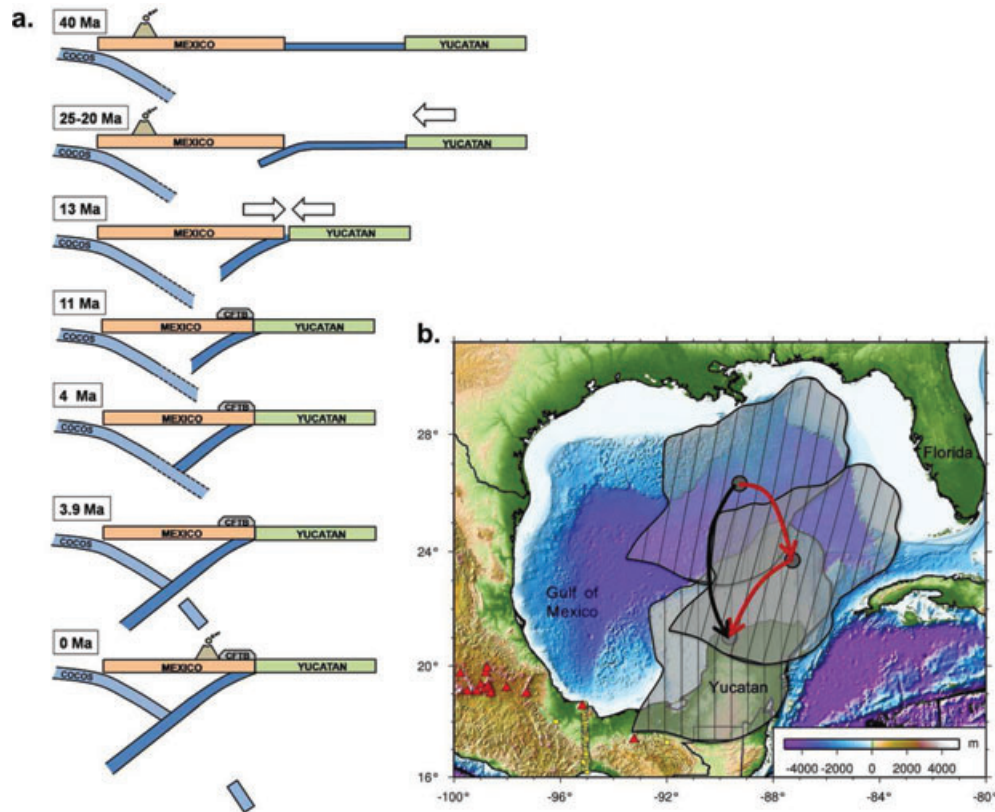
Figure 10. Proposed tectonic reconstruction diagram for southern Mexico. (a) A schematic model showing the collision of the Yucatán in Mexico. The onset of subduction (25–20 Ma) is estimated assuming a subduction rate of 2–5 cm yr^{-1} and a slab length of 250 km. The date of truncation of the Cocos slab is taken from Rogers *et al.* (2002). The volcanism is extinguished at the Miocene arc due to the collision, and reappears after 3 Ma (Manea & Manea 2008). The last stage at 0 Ma shows a present-day model for southern Mexico, and the volcano symbol indicates the MCVA. It is also directly analogous to Fig. 9(b). (b) Map view of the Yucatán Block rotations. The black line arrow represents the counter-clockwise movement of the Yucatán Block based on the standard model by Pindell & Kennan (2009). The red solid-line arrow represents our proposed model. We note that arrow positions are only indicative, not based on true tectonic reconstruction.

8 CONCLUSIONS

The RF image along the VEOX line in southern Mexico reveals the presence of the southwest-dipping structure (Yucatán slab) that descends to 250 km depth. The extent of this structure to the southeast is primarily supported by the RFs and tomographic images. A model with the Yucatán Block colliding with Mexico in the Miocene can explain the anomalous structures in the region. The proposed suture zone of this collision is the CFTB.

ACKNOWLEDGMENTS

REFERENCES

Ammon, C.J., Randall, G.E. & Zandt, G., 1990. On the nonuniqueness of receiver function inversions, *J. geophys. Res.,* **95**(B10), 15 303–15 318.

Andreani, L., Rangin, C., Martínez-Reyes, J., Le Roy, C., Aranda García, M., Le Pichon, X. & Peterson-Rodriguez, R., 2008. The Neogene Veracruz fault: evidences for left-lateral slip along the southern Mexico block, *Bull. Soc. géol. Fr.,* **179**(2), 195–208.

Billen, M.I., 2008. Modeling the dynamics of subducting slabs, *Annu. Rev. Earth planet. Sci.,* **36**(1), 325–356.

Bird, D.E., Burke, K., Hall, S.A. & Casey, J.F., 2005. Gulf of Mexico tectonic history: hotspot tracks, crustal boundaries, and early salt distribution, *Am. Assoc. Pet. Geol. Bull.,* **89**(3), 311–328.

Buffler, R.T., Schlager, W. & Pisciotto, K.A., 1984. Initial reports of the deep sea drilling project Leg 77, pp. 5–22.

Burbach, G.V., Frohlich, C., Pennington, W.D. & Matumoto, T., 1984. Seismicity and tectonics of the subducted cocos plate, *J. geophys. Res.,* **89**(B9), 7719–7735.

Campillo, M., Singh, S.K., Shapiro, N., Pacheco, J. & Hermann, R.B., 1996. Crustal structure of the Mexican volcanic belt based on group velocity dispersion, *Geofís. Int.,* **35**, 361–370.

Castro Artola, O.A., 2010. Caracterizacion de la geometria de la zona benioff con una red densa de banda ancha en el istmo de tehuantepec, *Ba thesis*, Universidad Nacional Autónoma de México.

Chen, T. & Clayton, R.W., 2010. Three-dimensional attenuation and velocity structure of the Cocos subduction zone in Mexico, in *Abstract DI31A-*

1943 presented at 2010 Fall Meeting, AGU, San Francisco, CA, 13–17 Dec.

Damon, P.E. & Montesinos, E., 1978. Late Cenozoic volcanism and metallogenesis over an active Benioff zone in Chiapas, Mexico, *Arizona Geol. Soc. Digest,* **X1,** 155–168.

Dickinson, W.R., 2009. The Gulf of Mexico and the southern margin of Laurentia, *Geology,* **37,** 479–481.

Ferrari, L., 2004. Slab detachment control on mafic volcanic pulse and mantle heterogeneity in central Mexico, *Geology,* **32**(1), 77–80.

Gaite, B., Villaseñor, A., Herraiz, M., Iglesias, A. & Pacheco, J.F., 2010. Ambient noise surface wave tomography in Mexico, Gulf of Mexico and Central America, in *Abstract S23B-06 presented at 2010 Fall Meeting, AGU*, San Francisco, CA, 13–17 Dec.

Gonzalez-Fernandez, A., Danobeita, J.J., Delgado Argote, L.A., Michaud, F., Cordoba, D. & Bartolome, R., 2005. Mode of extension and rifting history of the upper Tiburon and upper Delfin basins, northern Gulf of California, *J. geophys. Res.,* **110**(B01313), 1–17.

Gorbatov, A. & Fukao, Y., 2005. Tomographic search for missing link between the ancient Farallon subduction and the present Cocos subduction, *Geophys. J. Int.,* **160**(3), 849–854.

Guerrero, J.C., Herrero-Bervera, E. & Helsley, C.E., 1990. Paleomagnetic evidence for post-Jurassic stability of southeastern Mexico: Maya Terrane, *J. geophys. Res.,* **95**(B5), 7091–7100.

Hall, S.A. & Najmuddin, I.J., 1994. Constraints on the tectonic development of the eastern Gulf of Mexico provided by magnetic anomaly data, *J. geophys. Res.,* **99**(B4), 7161–7175.

Jacobsen, S.D. & van der Lee, S., 2006. *Earth's Deep Water Cycle*, American Geophysical Union, Washington, DC.

Kawakatsu, H. & Watada, S., 2007. Seismic evidence for deep-water transportation in the mantle, *Science,* **316,** 1468–1471.

Kennett, B.L.N. & Engdahl, E.R., 1991. Traveltimes for global earthquake location and phase identification, *Geophys. J. Int.,* **105**(2), 429–465.

Kikuchi, M. & Kanamori, H., 1982. Inversion of complex body waves, *Bull. seism. Soc. Am.,* **72**(3), 491–506.

Kim, Y., Clayton, R.W. & Jackson, J.M., 2010. Geometry and seismic properties of the subducting Cocos plate in central Mexico, *J. geophys. Res.,* **115**(B6), 1–22.

Langston, C.A., 1979. Structure under Mount Rainier, Washington, inferred from teleseismic body waves, *J. geophys. Res.,* **84**(B9), 4749–4762.

Li, C., van der Hilst, R.D., Engdahl, E.R. & Burdick, S., 2008. A new global model for *P* wave speed variations in Earth's mantle, *Geochem. Geophys. Geosyst.,* **9**(5), 1–21.

Ligorria, J.P. & Ammon, C.J., 1999. Iterative deconvolution and receiver-function estimation, *Bull. seism. Soc. Am.,* **89**(5), 1395–1400.

Mandujano-Velazquez, J. & Keppie, J.D., 2009. Middle Miocene Chiapas fold and thrust belt of Mexico: a result of collision of the Tehuantepec Transform/Ridge with the Middle America Trench, *Geol. Soc. Spec. Publ.,* **327,** 55–69.

Manea, M. & Manea, V.C., 2008. On the origin of El Chichón volcano and subduction of Tehuantepec Ridge: a geodynamical perspective, *J. Volc. Geotherm. Res.,* **175**(4), 459–471.

Manea, M., Manea, V., Ferrari, L., Kostoglodov, V. & Bandy, W., 2005. Tectonic evolution of the Tehuantepec Ridge, *Earth planet. Sci. Lett.,* **238**(1-2), 64–77.

Manea, V. & Manea, M., 2006. Origin of the modern Chiapanecan Volcanic arc in southern Mexico inferred from thermal models, *Geol. Soc. Am.* Sp. Paper, **412,** 27–38.

Marton, G. & Buffler, R.T., 1994. Jurassic reconstruction of the Gulf of Mexico Basin, *Int. Geol. Rev.,* **36,** 545–586.

Melgar, D., 2009. El proceso de subducción en la zona del Istmo de Tehuantepec a partir de funciones receptor, *Phd thesis,* Universidad Nacional Autónoma de México.

Melgar, D. & Pérez-Campos, X., 2010. Imaging the Moho and subducted oceanic crust at the Isthmus of Tehuantepec, Mexico, from receiver functions, *Pure appl. Geophys.,* **168**(8-9), 1449–1460.

Mora, J., Jaimes-Viera, M., Garduño Monroy, V., Layer, P., Pompa-Mera, V. & Godinez, M., 2007. Geology and geochemistry characteristics of the Chiapanecan Volcanic Arc (Central Area), Chiapas Mexico, *J. Volc. Geotherm. Res.,* **162,** 43–72.

Mullins, H., Gardulski, A., Wise, S. & Applegate, J., 1987. Middle Miocene oceanographic event in the eastern Gulf of Mexico: implication for seismic stratigraphic succession and Loop Current/Gulf Stream circulation, *Geol. soc. Am. Bull.,* **98,** 702–713.

Pardo, M. & Suárez, G., 1995. Shape of the subducted Rivera and Cocos plates in southern Mexico: Seismic and tectonic implications, *J. geophys. Res.,* **100**(B7), 12 357–12 373.

Pérez-Campos, X. et al., 2008. Horizontal subduction and truncation of the Cocos Plate beneath central Mexico, *Geophys. Res. Lett.,* **35**(18), 1–6.

Pindell, J. & Dewey, J.F., 1982. Permo-Triassic reconstruction of western Pangea and the evolution of the Gulf of Mexico/Caribbean region, *Tectonics,* **1**(2), 179–211.

Pindell, J. & Kennan, L., 2009. Tectonic evolution of the Gulf of Mexico, Caribbean and northern South America in the mantle reference frame: an update, *Geol. Soc. Lond. Spec. Publ.,* **328**(2009), 1–55.

Rebollar, C.J., Espíndola, V.H., Uribe, A., Mendoza, A. & Pérez-Vertti, A., 1999. Distributions of stresses and geometry of the Wadati-Benioff zone under Chiapas, Mexico, *Geofis. Int.,* **38,** 95–106.

Rogers, R., Karason, H. & van der Hilst, R.D., 2002. Epeirogenic uplift above a detached slab in northern Central America, *Geology,* **30**(11), 1031–1034.

Savage, M.K., 1998. Lower crustal anisotropy or dipping boundaries? Effects on receiver functions and a case study in New Zealand, *J. geophys. Res.,* **103,** 15 069–15 087.

Syracuse, E.M. & Abers, G.A., 2006. Global compilation of variations in slab depth beneath arc volcanoes and implications, *Geochem. Geophys. Geosyst.,* **7**(5), 1–18.

Verma, S.P., 2006. Extension-related origin of magmas from a garnet-bearing source in the Los Tuxtlas volcanic field, Mexico, *Int. J. Earth Sci.,* **95,** 871–901.

Vinnik, L.P., 1977. Detection of waves converted from P to SV in the mantle, *Phys. Earth planet. Inter.,* **15,** 39–45.

Wada, I. & Wang, K., 2009. Common depth of slab-mantle decoupling: reconciling diversity and uniformity of subduction zones, *Geochem. Geophys. Geosyst.,* **10**(Q10009), doi:10.1029/2009GC002570.

Waldhauser, F. & Ellsworth, W.L., 2000. A double-difference earthquake location algorithm: method and application to the Northern Hayward Fault, California, *Bull. seism. Soc. Am.,* **90**(6), 1353–1368.

Worzel, J.L., 1973. *Initial Reports of the Deep Sea Drilling Project Leg 10*, Vol. **25,** pp. 3–6, Washington, U.S. Government Printing Office.

Yuan, X. et al., 2000. Subduction and collision processes in the Central Andes constrained by converted seismic phases, *Nature,* **408,** 958–961.

Zamora-Camacho, A., Espindola, V.H., Pacheco, J.F., Espindola, J.M. & Godinez, M.L., 2010. Crustal thickness at the Tuxtla Volcanic Field (Veracruz, Mexico) from receiver functions, *Phys. Earth planet. Inter.,* **182**(1-2), 1–9.

Zarifi, Z., Havskov, J. & Hanyga, A., 2007. An insight into the Bucaramanga nest, *Tectonophysics,* **443**(1-2), 93–105.

Zhu, L. & Kanamori, H., 2000. Moho depth variation in southern California from teleseismic receiver functions, *J. geophys. Res.,* **105**(B2), 2969–2980.